PAPER

Simulation of pellet ELM triggering in low-collisionality, ITER-like discharges

To cite this article: A. Wingen *et al* 2021 *Nucl. Fusion* **61** 126059

View the article online for updates and enhancements.

Simulation of pellet ELM triggering in low-collisionality, ITER-like discharges

A. Wingen[1],[*] , B.C. Lyons[2] , R.S. Wilcox[1] , L.R. Baylor[1], N.M. Ferraro[3],
S.C. Jardin[3] and D. Shiraki[1]

[1] Oak Ridge National Laboratory, Oak Ridge, TN 37831, United States of America
[2] General Atomics, PO Box 85608, San Diego, CA, United States of America
[3] Princeton Plasma Physics Laboratory, PO Box 451, Princeton, NJ 08543, United States of America

E-mail: wingen@fusion.gat.com

CrossMark

Abstract

3D nonlinear, as well as 2D linear M3D-C1 simulations are used to model ELM triggering by small pellets in DIII-D discharges in the ITER relevant, peeling-limited pedestal stability regime. A critical pellet size threshold is found in both experiment and modeling depending on pedestal conditions, pellet velocity and injection direction. Using radial injection at the outboard midplane, the threshold is determined by M3D-C1 for multiple time slices of a DIII-D low-collisionality discharge that has pellet ELM triggering. Experimental observations show that a larger pellet size than the standard 1.3 mm diameter is necessary for ELM triggering; 1.8 mm pellets triggered several ELMs in cases where a smaller pellet failed. The M3D-C1 simulations are in good agreement with these observations. While the 2D linear simulations give insight into the change of growth rates for various toroidal modes with pellet size, the 3D nonlinear simulations apply a pellet ablation model that mimics the actual injection with good match to the experiment. The 3D nonlinear simulation confirms the pellet ELM triggering for a pellet size larger than the threshold found by the linear simulations.

Keywords: pellet, ELM triggering, M3D-C1, DIII-D, tokamak

(Some figures may appear in colour only in the online journal)

1. Introduction

Transient control is a critical issue for ITER and other future fusion burning plasma devices. Edge localized mode (ELM) mitigation or suppression in particular is essential to prevent significant damage, like melting, of plasma facing components. Even the unmitigated, axisymmetric, steady-state heat flux in ITER [1] is predicted to heat the water-cooled tungsten (W) monoblock divertor target plate tile surfaces to well above their melting temperature [2]. Therefore, ITER has to operate in partially detached divertor scenarios [3] to limit the incident heat flux to 10 MW m^{-2}. Transients like unmitigated ELMs, however, will likely burn through the detachment, causing the incident heat flux to significantly exceed that limit [4].

Various methods of ELM control have been studied on multiple machines. 3D resonant magnetic perturbations have been routinely applied in tokamaks to mitigate or suppress ELMs [5–7]. These results motivated the inclusion of an in-vessel, non-axisymmetric, control coil set in the ITER baseline design [8]. Another very promising method available in ITER is ELM pacing by injecting cryogenically frozen deuterium pellets at a frequency higher than the natural ELM frequency [9]. Previous studies on DIII-D [10–12], ASDEX Upgrade [13] and JET [14, 15], have demonstrated that triggering ELMs on demand by pellet injection at a frequency higher than that of the naturally occurring ELMs can reduce the peak instantaneous heat flux incident on the divertor target.

Traditionally, experiments exploring pellet ELM pacing have operated in regimes with high collisionality [16] in the pedestal region, $\nu^*_{\text{ped}} \gtrsim 2$, due to the difficulty of achieving low

density edge plasma conditions while injecting pellets [11, 12]. The pedestal stability of such high-collisionality discharges is typically limited by ballooning instabilities that are driven by the edge pressure gradient. Since it is the general understanding that pellets trigger ELMs by providing a pressure perturbation in the plasma [11, 17], it is beneficial for pellet ELM triggering to operate close to the ballooning stability limit. Further experiments include studies of pellet material drift [18–20], which can affect ELM triggering and fueling.

ITER, however, is predicted to operate at very low collisionality in the pedestal region, $\nu^*_{\mathrm{ped}} \sim 0.2$ [21]. Thus, the pedestal stability in ITER will be limited by peeling instabilities, driven by the edge current density. To demonstrate and predict the feasibility of pellet ELM triggering in ITER, it is necessary to study it in present-day machines under low-collisionality conditions. Recently such experiments have been performed at DIII-D [22] and are studied numerically in this publication.

To simulate pellet ELM triggering we use the M3D-C1 code [23], an implicit, high-order finite-element code, that solves linear [24] and nonlinear extended magneto-hydrodynamic (MHD) equations in magnetized toroidal geometry. Recently, M3D-C1 has been coupled to the KPRAD-model for impurity dynamics, allowing the MHD solution to evolve self-consistently with ionization, radiation, recombination, and transport of impurity species [25]. Such simulations have been benchmarked to similarly coupled NIMROD [26, 27] simulations, showing excellent agreement [28]. Furthermore, a model for the injection and ablation of mixed deuterium-neon cryogenic pellets has been implemented in M3D-C1 for the simulation of disruption mitigation by shattered-pellet injection. Pellet ELM triggering has also been recently studied in nonlinear MHD simulations using the JOREK code [17, 29].

The paper is organized as follows. The next section lays out the numerical setup of the M3D-C1 simulations with pellets, used throughout this paper. Section 3 shows the results of linear modeling to determine the pellet size threshold for ELM triggering, and shows its dependence on location and pedestal collisionality conditions. In section 4 thresholds are then simulated for multiple times and compared to events of failed or successful pellet ELM triggering in the experiment. Results of a fully 3D nonlinear simulation, which confirms a successful triggering of an ELM by a pellet larger than the previously determined threshold, are discussed in detail in section 5. The paper is finalized by the conclusions in section 6.

2. Numerical setup

M3D-C1 uses a kinetic EFIT equilibrium [30] along with 1D electron density, electron temperature and $E \times B$ rotation profiles (see figure 10 for details) to initialize the background plasma. In the following we focus on DIII-D discharge 178555, an H-mode plasma with a modified ITER-similar shape; the outer strike point has been pulled radially inward (see figure 6 for details). The discharge has 1.8 MW of co-directed neutral beam heating, 1.5 MW of centrally deposited ECH, a toroidal field of $B_{\mathrm{t}} = 1.6$ T, a plasma current of

$I_{\mathrm{p}} = 1.1$ MA, $q_{95} = 4.4$, and is low pedestal collisionality with $\nu^* < 1$.

In the simulation the pellet is added as an additional main-ion density source S to the continuity equation, positioned at the injection location $(R_{\mathrm{p}}, \varphi_{\mathrm{p}}, Z_{\mathrm{p}})$, and localized by a 2D Gaussian of width v_{p} in the R–Z plane

$$S_{\mathrm{2D}} = \frac{1}{2\pi R v_{\mathrm{p}}^2} \exp\left(-\frac{(R - R_{\mathrm{p}})^2 + (Z - Z_{\mathrm{p}})^2}{2v_{\mathrm{p}}^2}\right) \quad (1)$$

and a periodic von Mises distribution of toroidal width v_{t}, which is essentially a 'periodic Gaussian' distribution along the toroidal angle in cylindrical coordinates, resulting in

$$S = S_{\mathrm{2D}} \cdot \frac{R}{\sqrt{2\pi} v_{\mathrm{t}}} \exp\left(-\frac{R R_{\mathrm{p}}(1 - \cos(\varphi - \varphi_{\mathrm{p}}))}{v_{\mathrm{t}}^2}\right). \quad (2)$$

In the following we use M3D-C1 in single-fluid, linear-2D mode as well as in nonlinear-3D mode. The latter will be discussed in more detail in section 5. In linear-2D we identify $S = S_{\mathrm{2D}}$ only, which implicitly turns the pellet into an axisymmetric density ring instead of a toroidally localized pellet. Furthermore in contrast to nonlinear-3D, in linear-2D simulations the equilibrium and pellet do not move or evolve in time, but are a frozen snap shot, which is then analyzed for linear stability as a time-dependent, initial value problem, for one toroidal mode number at a time. In summary, the pellet causes a stationary, axisymmetric density perturbation to the axisymmetric equilibrium, while the linear-2D simulation shows if that perturbation is large enough to drive linear instability.

M3D-C1 utilizes a mesh in the R–Z plane, which has been adapted to the initial equilibrium. Figure 1 shows the mesh in the poloidal cross section. The equilibrium's separatrix is given by the red line. The blue and green lines represent a resistive wall that is part of the simulation domain [31]. The mesh is most dense near the separatrix but then becomes coarse in the scrape-off-layer (SOL) and even more so in the vacuum region outside the wall. Note that the MHD equations are not evolved in the resistive wall or vacuum region. The magnification on the right shows the outer midplane with the pellet as the Gaussian density perturbation just inside the separatrix. For the linear-2D simulations only four inputs are needed to set up the pellet: the position $(R_{\mathrm{p}}, Z_{\mathrm{p}})$, the Gaussian width of the pellet v_{p} (see equation (1)), and the magnitude of the density perturbation. The latter is called the 'pellet-rate' A_{p}, which is a dimensionless factor, which technically allows for multiple pellets and therefore a time variation. Since we only use a single pellet, we keep the name but here it is scaling the amplitude of the Gaussian in equation (1).

In order to determine the proper values for the pellet input, an ablation model is used [32]. Assuming the pellet is injected radially at $Z = 0$ on the low-field-side (LFS), the model calculates where a deuterium pellet of a given size ablates in the plasma. This provides the radial location R_{p} and the Gaussian width v_{p}. However, the stand alone ablation model fully ablates the pellet and is therefore not suitable to set the pellet-rate A_{p}. Nonlinear M3D-C1, which uses the same ablation model, ablates the pellet over time self-consistently with the plasma
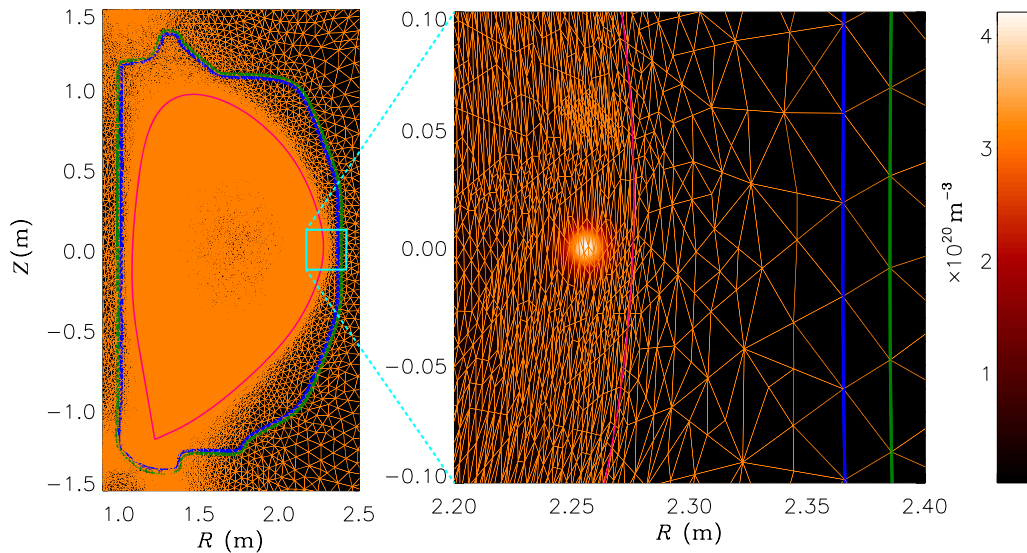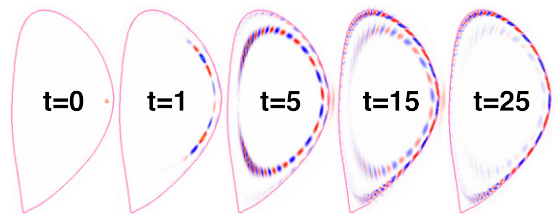
Figure 1. Left: poloidal cross section of the M3D-C1 mesh within the simulation domain. The separatrix is given by the red line. The resistive wall is given by the blue and green lines. Right: magnification of the outboard midplane, showing the pellet density.
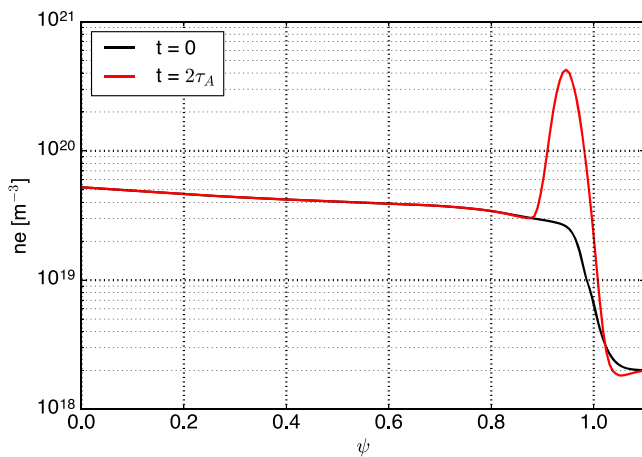
Figure 2. Electron density along the minor radius, given by the normalized poloidal flux ψ, at $Z = 0$ from the magnetic axis outwards. Black: without pellet, red: with pellet ablation, note that the y-axis is on a log scale.

Figure 3. Temporal evolution of $n = 9$ mode structures within the plasma after an initial perturbation by a pellet of size 0.72 mm, injected at the outboard midplane. The time is measured in Alfven time.

simulation; the pellet-rate is thereby calculated by M3D-C1 at each time step of the simulation. So, we run a 3D nonlinear simulation with low toroidal resolution (here 8 planes are used) for only a few Alfven times to determine the peak density, as shown in figure 2. The black line is the background electron density along the plasma's minor radius, given by the normalized poloidal flux ψ, from the magnetic axis outwards at $Z = 0$, while the red line shows the peak caused by the ablating pellet. The spatial ablation profile is well reflected by the peak location of the density profile. In the linear runs the code inputs are set so that the density perturbation matches the peak shown in figure 2. For a spherical pellet of radius $r_p = 0.72$ mm, we find $R_p = 2.256$ m, $Z_p = 0$, $v_p = 0.0072$ and $A_p = 0.0029$. The latter results in a peak electron density of 4.24×10^{20} m^{-3}. The magnification on the right side of figure 1 shows the pellet density perturbation using those input parameters. Note that

in the linear simulations the perturbation is adiabatic, i.e. the temperature is reduced while the pressure remains fixed.

While the input equilibrium is MHD stable, a pellet-induced perturbation of significant size can cause the plasma to become linearly unstable, resulting in an ELM. Figure 3 shows a simulation to illustrate that process. At $t = 0$ the pellet perturbes the plasma at the outboard midplane. For $t > 0$ a mode grows on the perturbed flux surface and starts spreading poloidally; here a mode with toroidal mode number $n = 9$ is shown. Note that the poloidal mode number is determined by the local $q = m/n$ value. With time progressing, the mode on the flux surface decays away, while another mode starts growing just inside the separatrix, indicating an unstable ballooning response. Eventually this linear mode would begin to interact nonlinearly with modes of other toroidal numbers, resulting in the nonlinear ELM crash. Such nonlinear coupling is outside the scope of this linear modeling, but will be examined in section 5.

3. Pellet size threshold for ELM triggering

In this section we use linear-2D M3D-C1 simulations to determine the linear stability of the plasma when pellets of various sizes are injected. Since the simulations are linear, each

toroidal mode n can be simulated individually. To cover a typical range of low to intermediate to high n modes, a total of 14 simulations for $n = 1, 2, 3, 5, 7, \ldots, 25$ are performed for each pellet size. By sampling pellet sizes between 0.5 mm to 1.44 mm, which covers the range of experimentally used pellets in DIII-D, the pellet size threshold for ELM triggering can be determined. Note that 'pellet size' in this context stands for the radius r_p of a spherical pellet. Pellets used in experiments are cylindrical where typically the length L equals the diameter d. Assuming equal volume the conversion is given by

$$d = L = (16/3)^{1/3} r_p \approx 1.747 r_p. \tag{3}$$

For the analysis in this section we focus on time slice 3055 ms of DIII-D discharge 178555 for now. In section 4 the same procedure is then applied to further time slices of the same discharge.

3.1. Finding a threshold

Each M3D-C1 simulation is run for at least 300 Alfven times τ_A (6.48×10^{-7} s for parameters in this simulation) to saturate the linear growth rates of the modes. Note that neither the background equilibrium, nor the pellet density perturbation itself is evolving during the simulation. Only the perturbations, caused by the pellet as well as an initial random perturbation of small relative magnitude to the single-fluid MHD variables, evolve over time.

Figure 4 shows the linear growth rate γ for the least stable eigenmode versus the toroidal mode number n for the equilibrium without pellet injection (black line) as well as five different pellet sizes. Each marker represents a linear M3D-C1 simulation. Note that for each pellet size the poloidal width v_p as well as the pellet-rate A_p are changed consistent to the pellet volume, while the position (R_p, Z_p) is kept fixed. As can be seen in the figure, the plasma is stable without pellet injection as well as for pellet sizes of 0.5 mm (red line) and 0.61 mm (blue line) with growth rates below zero, indicated by the dashed line. For pellet size 0.72 mm (green line) the growth rate is greater than zero for $n = 9$ and $n = 11$, resulting in unstable modes that could lead to an ELM. For larger pellets, 0.9 mm (purple line) and 1.44 mm (cyan line) more modes in the intermediate n-range become unstable with increasing growth rates. The most unstable mode is found to be around $n = 9$. The intermediate range of n-modes that show positive growth rates suggests that the plasma becomes peeling unstable, meaning that the pedestal stability is limited by the edge current density rather than the pressure gradient (ballooning unstable); the latter is typically associated with larger n-modes of $n \gtrsim 20$.

Using the growth rates for the most unstable mode in figure 4, $n = 9$, for all simulated pellet sizes, the critical pellet size threshold for ELM triggering can be interpolated, as shown in figure 5. The markers represent the growth rates, as found in the previous figure for the respective pellet sizes. The black line is a modified tanh, a tanh with linear asymptotics, fitted to the data points. The zero-crossing, given by the dashed line, then sets the critical pellet size threshold. The latter is found as $r_{crit} = 0.7018$ mm for this time slice. So, we expect
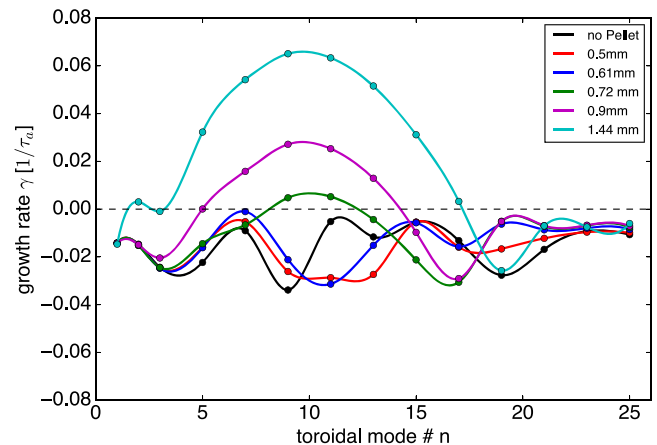
Figure 4. Linear growth rates of toroidal modes between $n = 1$ and $n = 25$ for multiple pellet sizes, injected into discharge 178555 at 3055 ms.
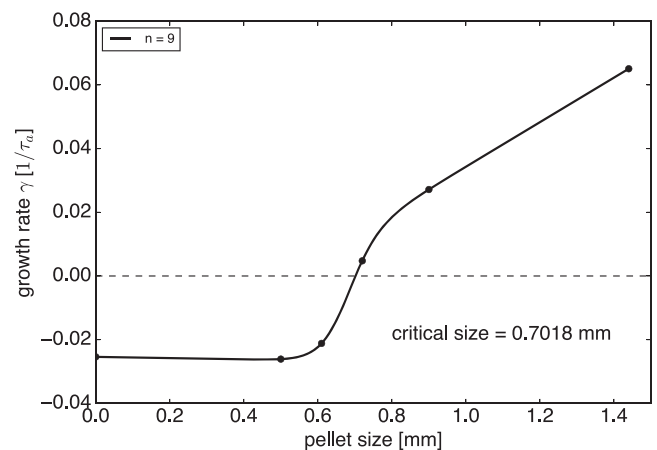

Figure 5. Linear growth rate dependence on pellet size for the most unstable mode, $n = 9$, in figure 4. The pellet size is the radius of a spherical pellet.

that pellets larger than r_{crit} can successfully trigger an ELM in this discharge at this time, while smaller ones cannot.

3.2. Threshold vs poloidal injection location

The pellets in the previous subsection have been injected at the outboard midplane, given by $Z_p = 0$, further on identified as the 0° location. In this section we vary the poloidal injection location, while maintaining the same flux surface location as in the 0° case, given by $\psi_p = 0.945$. Note that the linear simulations do not include any pellet motion, therefore the direction of pellet injection has no direct impact on the shown results. Since the outboard midplane injection is considered to be radially inwards, we maintain the assumption that pellets move perpendicular to the flux surfaces towards the magnetic axis for the other poloidal locations. Furthermore, linear M3D-C1 does not account for the drift of particles ablated by the pellet in the edge. It has been observed that such drifts could either transport pellet material further into the plasma, as seen on the HFS, increasing the so called fueling efficiency, or out
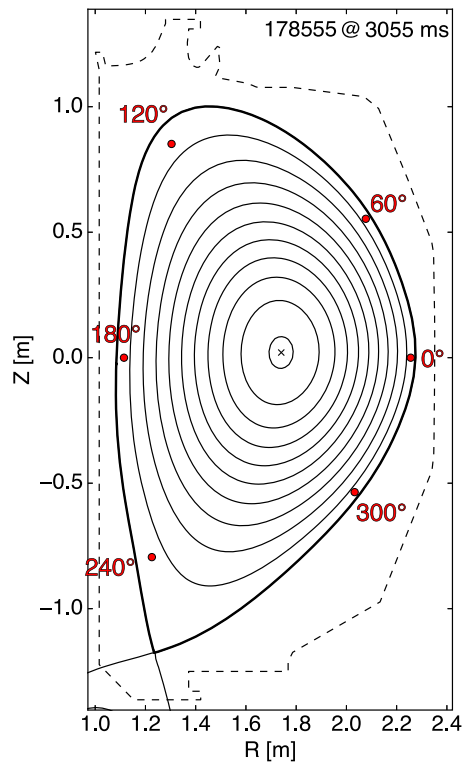
Figure 6. Poloidal cross-section of discharge 178555 at 3055 ms. The red dots show the location of pellet injection.

Figure 7. Pellet size thresholds for ELM triggering depending on the poloidal injection location, as shown in figure 6.

into the SOL, as has been seen on the LFS, especially the midplane [18]. Such a drift can affect the effective pellet size necessary to trigger ELMs, as material can be moved towards or away from the critical location for ELM triggering. Therefore, we point out that 'pellet size' here refers to the actual plasma perturbation size.

Figure 6 shows the poloidal cross-section of discharge 178555 at 3055 ms with the red markers showing the various poloidal injection locations considered here. For each of these locations the critical pellet size threshold is determined using the same procedure as discussed above. As shown in figure 7 the critical pellet size threshold, shown by the blue markers, varies significantly with the poloidal injection location. The $0°$ and $60°$ locations have similarly small thresholds around 0.7 mm, which makes them the most effective locations for ELM triggering. At $120°$ and $240°$, which is near the upper and lower x-points respectively, the threshold exceeds 1.5 mm and has not been determined any further. At $180°$ and $300°$ the threshold is about 1.31 mm. Keep in mind that a factor of two in pellet size translates into a factor of eight increase in the pellet's mass and number of particles.

The reason why the outboard midplane is among the most effective locations is generally to be believed due to a strong coupling with ballooning modes in that region. Injected pellets cause a large local increase in density when ablating. Even though this causes a drop in local temperature due to dilution cooling, the pressure still spikes, because parallel electron thermal transport is much faster than the ion sound speed. The working hypothesis in the pellet community, as also shown in section 5, is that this increase in pressure then
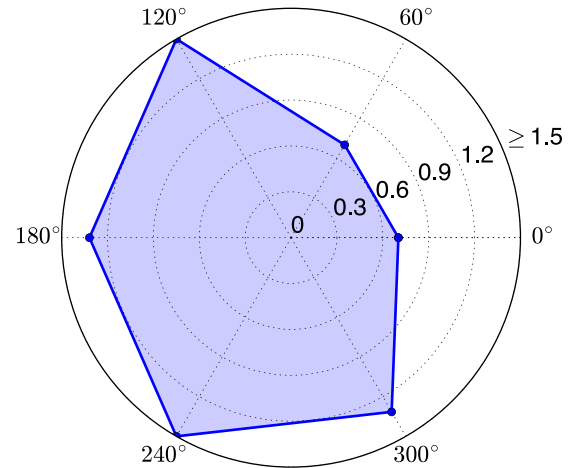
kicks the equilibrium over the ballooning (pressure-gradient-limited) pedestal stability limit and triggers the ELM. Even for a peeling-limited pedestal, the increased density from the pellet pushes the pedestal into a ballooning regime. The increased threshold at the inboard midplane as well as the strong stability near the x-points agree with that hypothesis. The strong asymmetry between the $60°$ and the $300°$ locations is unexpected and still under investigation. The ITER pellet injection ports are located around $280°$, $225°$ and $210°$, which are in a section of significantly higher threshold here.

Previous experiments in DIII-D high-collisionality discharges [18] observe that ELMs triggered by low-field side (LFS) injection are much larger than ELMs triggered by high-field-side (HFS) injection for the same pellet size. Therefore the reference concludes that ELMs could be triggered by smaller pellets on the LFS than on the HFS. However, it should be pointed out that all pellets actually triggered ELMs in the experiment, so it is difficult to draw a clear conclusion on poloidal location. On the other hand, JOREK simulations of pellet ELM triggering suggest that HFS injection would require smaller pellets to trigger ELMs than LFS injection [17]. Furthermore, recent JET results show that the likelihood of triggering ELMs during pacing experiments is larger for vertical HFS (VHFS) injection than for LFS injection [33]. Note that the reference uses an extensive database of JET results which spans a wide range of electron density and temperature, but it does not distinguish by collisionality. Nevertheless, both results indicate that a VHFS location is more favorable for pellet injection. This important issue will be further addressed by future experiments in DIII-D with low collisionality plasmas, various pellet sizes and multiple injection locations.

3.3. Radial pellet penetration sensitivity

So far, all pellets were injected at the same radial flux surface location $\psi_p = 0.945$, which matches $(R_p, Z_p) = (2.256, 0)$ m at the outer midplane, as determined by the ablation model in figure 2. In this subsection we study how sensitive is the critical pellet size threshold to the radial location; the original point is
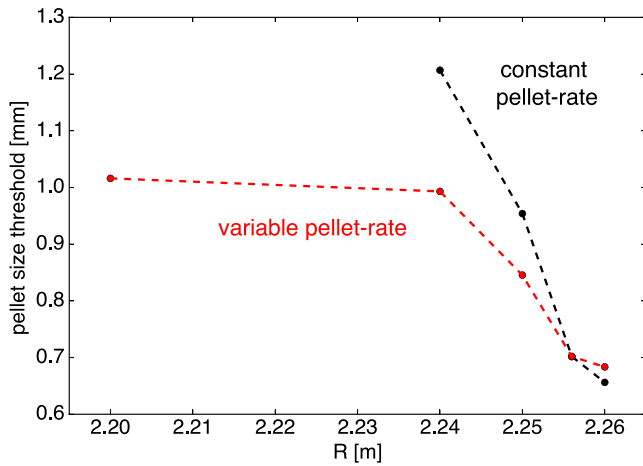
Figure 8. Pellet size thresholds for ELM triggering depending on radial location R_p along $Z = 0$. Black: constant pellet-rate, as found for $R_p = 2.256$. Red: pellet-rate is adjusted to respective radial position. Note that the separatrix is located at about 2.275 m.


Figure 9. ELITE stability diagram for discharge 178555 at 3055 ms. The black marker shows the operational point of the discharge. The red and blue markers are VARYPED equilibria along the same iso-stability surface. The black line marks the peeling-ballooning stability boundary.

used as reference. First, only R_p is changed in the code input, while all other inputs, $Z_p = 0$, v_p and A_p are kept fixed for pellets of the same size. This results in the black curve in figure 8. The critical pellet size threshold raises strongly with decreasing R_p, and drops further outwards of the reference point. This does not take into account, however, how the density and temperature of the background plasma, and thus the pellet-rate A_p, change as the pellet changes position.

The red curve in figure 8 takes the local change of the pellet-rate into account, which means that the pellet's density perturbation is larger in magnitude for the same pellet size the further inwards the pellet ablates. So, for the red curve not only R_p is changed, but also A_p in a consistent way to account for the local changes in the background plasma at the respective positions. The critical pellet size threshold still increases with decreasing R_p, but much more moderately, and drops less outwards of the reference point. Even if the radial position were unknown, the critical pellet size threshold would be within 0.85 mm $\pm 20\%$ across the entire plasma edge.

3.4. Peeling vs ballooning limited discharges

Discharge 178555 is a low collisionality discharge with $\nu^* < 1$ and with $\nu^* = 0.8$ at 3055 ms in particular. We expect the pedestal stability of the discharge to be limited by the edge current density (peeling) rather than by the pressure gradient (ballooning). This can be confirmed by the ELITE code [34] which calculates the pedestal stability diagram, as shown in figure 9. ELITE was run from within OMFIT [35]. The x-axis represents the normalized pressure gradient, the y-axis the normalized edge current density. The color contour where the diamagnetic stabilization is equal to one, given by the solid black line, denotes where the ideal peeling-ballooning instability overcomes diamagnetic stabilization and would result in an ELM crash. The black marker shows the operating point of the discharge at 3055 ms within the stable region, close to the horizontal branch of the stability boundary. So the pedestal stability is peeling limited here.
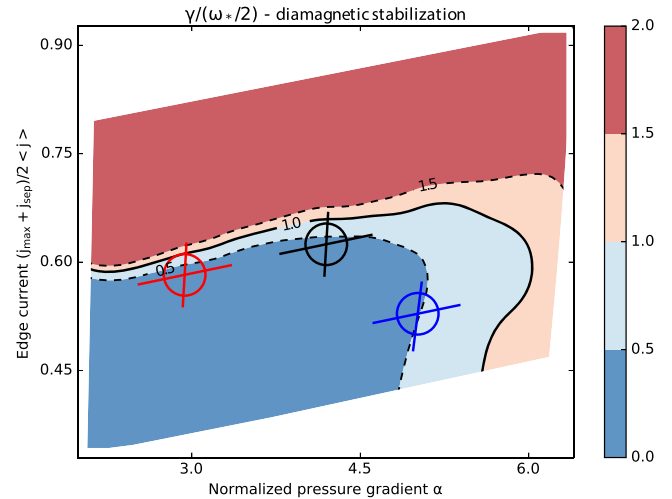
As mentioned earlier, the hypothesis for pellet ELM triggering is that the local pressure increase, due to the ablating pellet, pushes the operational point across the ballooning branch of the pedestal stability boundary. In other words, the pellet shifts the operational point more or less horizontally in the ELITE diagram. So, one would expect that the horizontal 'distance' of the operational point from the ballooning branch affects the pellet size threshold for ELM triggering. To test this hypothesis we use the VARYPED code to modify the electron density and electron temperature profiles to shift the operational point either more towards the ballooning branch (blue marker) or even further away to an even stronger peeling limited pedestal (red marker). Thereby the shift is done along the same iso-stability surface (given by the color contours) in figure 9.

Figures 10(*a*) and (*b*) show the electron density and electron temperature profiles respectively for all three cases, the original discharge at 3055 ms as well as the even stronger peeling limited case (red) and the ballooning limited case (blue). The profile variations are intended to scale the pressure gradient as well as the bootstrap current in the pedestal region so that the edge stability is systematically changed. Thereby, when scaling the pedestal pressure the core profiles are adjusted such that the total stored energy is fixed and roughly the collisionality profile is fixed. Also, when scaling the bootstrap current the total current is kept fixed. Note that there is no constraint on the central q value in this approach, which can lead to a q on axis below unity and therefore causing an $n = 1$ core instability in the simulation, as observed in the red curve in figure 11. The collisionality changes only moderately with the modified profiles; the peeling case has $\nu^* = 0.7$, while the ballooning case has $\nu^* = 1.1$. The plasma shape as well as the rotation profile and any other inputs to M3D-C1 remain unchanged.

Similar to figure 4 M3D-C1 then finds the linear growth rates for all the toroidal modes at a given pellet size of 0.72 mm for the peeling (red) and ballooning (blue) cases. Figure 11
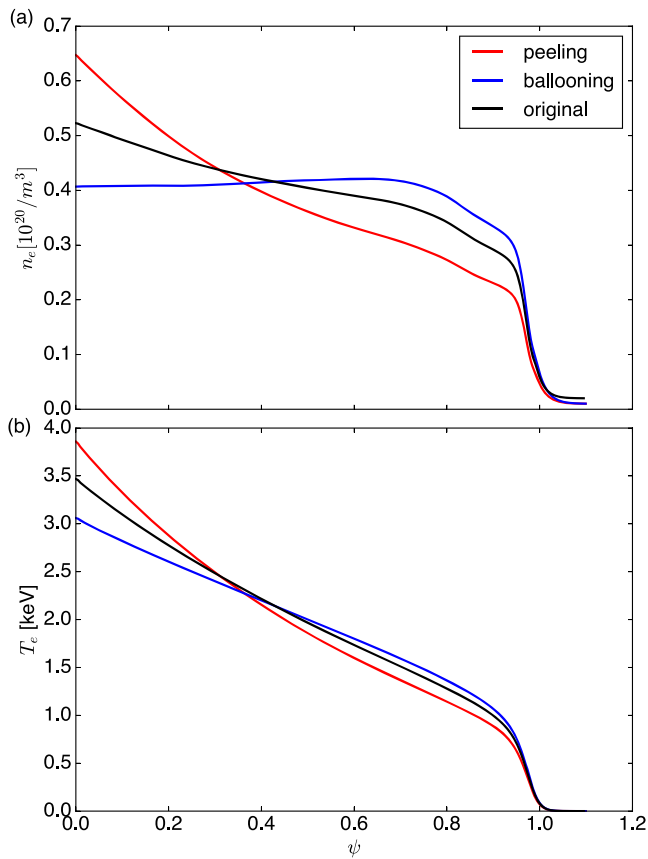
Figure 10. (*a*) Electron density and (*b*) electron temperature profile for 178555 at 3055 ms (black line), and its VARYPED variations according to figure 9.
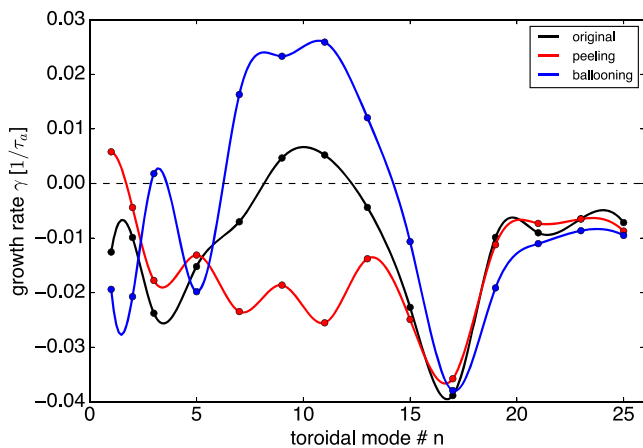
Figure 11. Linear growth rates for toroidal modes between $n = 1$ and $n = 25$ for the equilibria marked in figure 9, and a pellet size of 0.72 mm.

compares the results to the original discharge (black). Note that the black curve here is the same as the green curve in figure 4. While in the original discharge a 0.72 mm pellet just triggers an ELM with small but positive growth rates for $n = 9$ and $n = 11$, the ballooning limited case shows much larger growth rates for modes between $n = 7$ and $n = 13$. This shows that the ballooning limited case triggers an ELM much more easily and

therefore has a smaller critical pellet size threshold. The peeling limited case on the other hand shows negative growth rates for the same modes that are unstable in the other two cases. In this case a 0.72 mm pellet fails to trigger an ELM; the equilibrium remains stable in the edge, indicating that the pellet size threshold is greater than in the original discharge. The unstable $n = 1$ mode in this case is localized in the core and does not affect the edge stability. This result strongly supports the given hypothesis, but further experimental and theoretical research is needed to confirm it.

4. Comparison with experiment

In the experiment [22], cryogenically frozen deuterium pellets were injected at the outboard midplane directed towards the magnetic axis. Two sizes of cylindrical pellets were used, each produced using a separate pellet gun but launched from the same injection point inside the vessel. A traditionally pacing-sized pellet, with diameter 1.3 mm and length 0.9 mm, referred to as 'small' pellet from here on, is followed 20 ms later by a traditionally fueling-sized pellet, with diameter and length both 1.8 mm, henceforth referred to as 'big' pellet. Since the pellets are modeled as spherical in the simulation, an effective radius, which matches the pellet's volume, is found to be $r_p = 0.66$ mm for the small pellet and $r_p = 1.03$ mm for the big pellet. Note that the true mass (and number of macroscopic pieces) of each pellet can vary, due to differences in pellet quality produced by cutting pellets out of an extrusion as well as differential ablation along the guide tube; the latter is only a very weak effect.

Figure 12 shows time traces of the discharge evolution leading up to the first pellet injection: (*a*) the edge plasma density as measured by an interferometer cord through the outer radial regions of the confined plasma, (*b*) D_α emission in the divertor as measured by the filterscopes, (*c*) peak heat flux at the inner strike point from the infrared camera, (*d*) fluctuations in the magnetic field near the pellet injection location (that tend to coincide with ELMs), and (*e*) a photodiode signal measuring the pellet ablation light. Note that the last panel's *y*-axis is on a log scale. Leading up to the first pellet injection just after 3000 ms the discharge experiences large, slow, natural type-I ELMs at about 20 Hz frequency, as shown by the D_α signal. For each ELM the edge density drops, the infrared camera at the inner strike point records a spike in peak heat flux, and the magnetic probes register strong fluctuations. In between the ELMs the density recovers. After 3000 ms the pellet injection starts. A small pellet is followed by a big one 20 ms later. The consecutive injection of small and big pellets repeats every 200 ms, which is slower than the natural ELM frequency, to allow for the plasma to recover and the divertor cryopumps to remove the injected excess density, so that individual ELM triggering can be studied in contrast to high-frequency ELM pacing.

The vertical blue bar in figure 12 marks the ablation of the first small pellet, even though the peak in the photodiode signal is almost within the noise. The other signals, however, do not show the characteristics of an ELM at that time, so the small pellet fails to trigger. The big pellet then triggers an ELM 20 ms
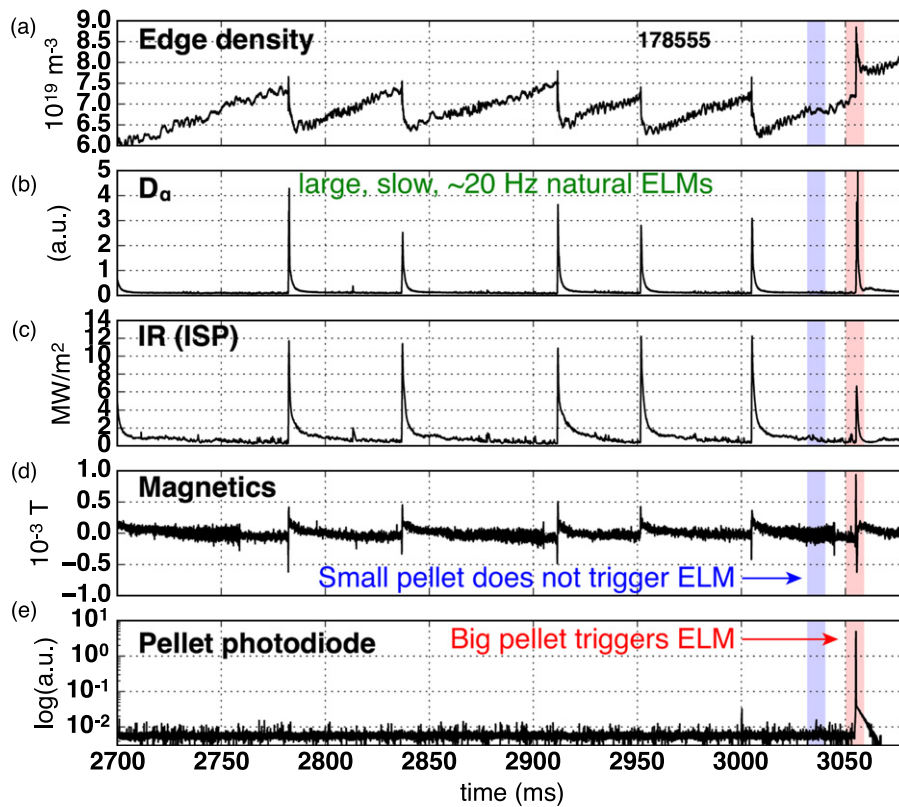
Figure 12. Time traces of discharge 178555, leading up to the first pellet injection: (*a*) the edge plasma density, (*b*) D_α emission in the divertor, (*c*) peak heat flux at the inner strike point, (*d*) magnetic fluctuations near the pellet injection location, and (*e*) a photodiode signal measuring the pellet ablation light.

later, identified by the spikes in all signals as highlighted by the vertical red bar. Also the ELM energy fluence changes for pellet triggered ELMs [22] like this, compared to natural ELMs. This observation repeats more or less throughout the discharge. Sometimes a small pellet triggers an ELM, but often it does not, while then the subsequent big pellet succeeds.

By applying the procedure discussed in section 3.1 to the times 2815, 3055, 3630, 3838, 4264, and 4434 ms, linear-2D M3D-C1 simulations found the critical pellet size thresholds at the respective times in discharge 178555. The results are shown in figure 13 by the black markers on top of the gray bars, which indicate the stable region of pellet sizes not triggering ELMs in the simulation. The variation in the thresholds is most likely due to the various timings of the equilibria within the respective ELM cycle of the pedestal. One would expect the threshold to be lower, if an equilibrium is closer in time to a natural ELM event. The thresholds are compared to events in the respective experiment. The red markers indicate when pellets fail to trigger an ELM, while the green markers indicate successful ELM triggering by the injected pellet. The shown size of each pellet is derived from the pellet mass, measured by a microwave cavity detector along the pellet path. The error bars give the uncertainty of the pellet size based on the microwave cavity detector background noise, which is quite asymmetric. The error is larger for small sizes and diminishes for larger pellets, due to the cubic relation between radius and mass. At 2815 ms no pellet is injected, but a natural ELM
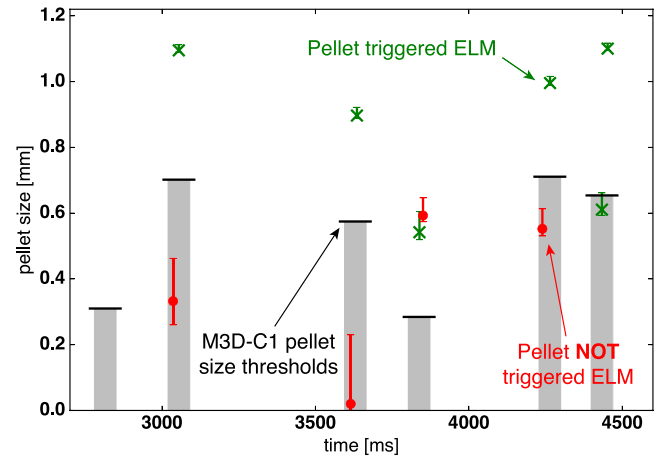

Figure 13. M3D-C1 simulated critical pellet size thresholds for multiple times in discharge 178555, shown by the gray bars, compared to events in the respective experimental discharge 178555: the red markers indicate when pellets fail to trigger an ELM, while the green markers indicate successful ELM triggering by the injected pellet.

occurs. This shows that there is still a finite pellet size threshold within the last 20% of the ELM cycle (the time average of the EFIT equilibrium) before a natural ELM event.

At 3055 ms the small pellet fails to trigger, and does not raise the density (see figure 12), as it is tiny and only a fragment of the desired pellet size. The big pellet succeeds. The
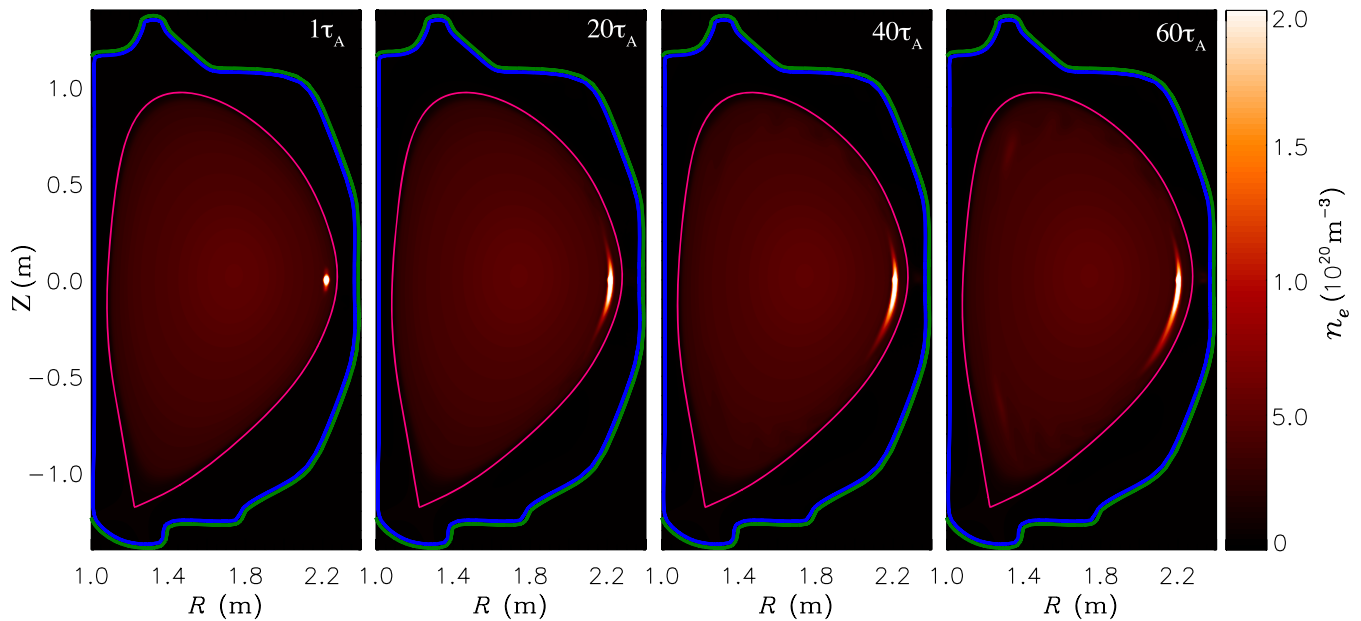
Figure 14. Electron density in the poloidal cross-section at $\varphi = 0$ for multiple times during the pellet ablation process.
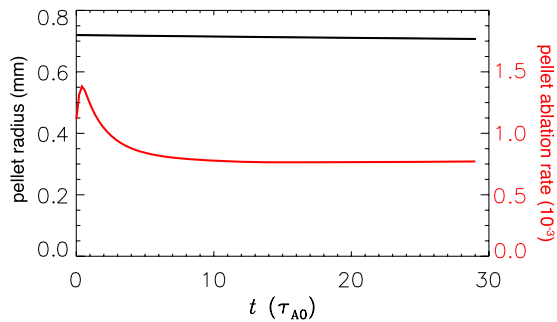
Figure 15. Time evolution of the pellet radius (black line) and the pellet-rate (red line).

simulated threshold of 0.7018 mm agrees with the experimental observation. At 3630 ms, only the large pellet is detected by the diagnostics, so the small pellet size is assumed to be within the detector noise. At 3838 ms a small pellet successfully trigges the ELM. Another small fragment follows right after, but does not trigger an additional ELM. Note that the shown threshold is calculated for an equilibrium right before the triggered ELM and does not capture the plasma state right after. At 4264 ms the situation is similar to earlier, where the small pellet fails, while the large one triggers the ELM. Finally at 4434 ms both pellets trigger an ELM. The threshold is clearly below the larger pellet size, while it is within the error bar of the smaller pellet size. Overall excellent agreement between simulation and experiment is found here.

5. 3D nonlinear simulation

In contrast to the linear simulations in the previous sections, fully 3D nonlinear M3D-C1 simulations evolve the plasma equilibrium as well as the pellet density source in time. The 3D simulations use a similar adaptive grid in the poloidal cross-section, see again figure 1, as the linear-2D ones, but with a slightly coarser grid resolution to reduce memory and computational time requirements. The grid is then extended toroidally using cubic finite elements for a given number of toroidal planes. The number of planes sets the limit on the toroidal modes that can be resolved. Here we use 48 planes, evenly distributed around the torus. Such a simulation is computationally very expensive and uses about 12k CPU cores to run for 36 h on the NERSC high-performance computing clusters in order to advance the time evolution for about 60 Alfven times. For the case discussed in this section, we use the equilibrium 178555 at 3055 ms, the same one used throughout section 3.

The code uses the same ablation model as shown in figure 2 to determine the pellet-rate, which now evolves in time. Therefore A_p is no longer a required input. Instead the pellet material, which is set to deuterium here, the pellet radius $r_p = 0.72$ mm, the initial size of the pellet cloud, set to 10 times the pellet radius to match v_p, and the local electron temperature and density are used to calculate the pellet-rate during the simulation. In contrast to the 2D-linear simulations the pellet density source S is also toroidally localized using equation (2). The toroidal width v_t of the von Mises distribution is set to $v_t = 0.45$ so that it can be reasonably resolved by the number of toroidal planes. Note that this means the full width of the toroidal distribution at half amplitude is about $26°$ or about 1 m at R_p. The initial pellet location is the same as in the linear-2D cases with $R_p = 2.256$ m, $Z_p = 0$ and now $\varphi_p = 0$. The pellet also moves with a given velocity $\vec{v} = (v_R, v_\varphi, v_Z) = (-500, 0, 0)$ m s^{-1} radially inwards. Note that in the actual experiment the pellet velocity ranges from 100 m s^{-1} to 400 m s^{-1}, while experimental observations show that the velocity dependence of ELM triggering is very weak. Therefore we use it here to shorten the computational time required to propagate the pellet within the edge; we run the
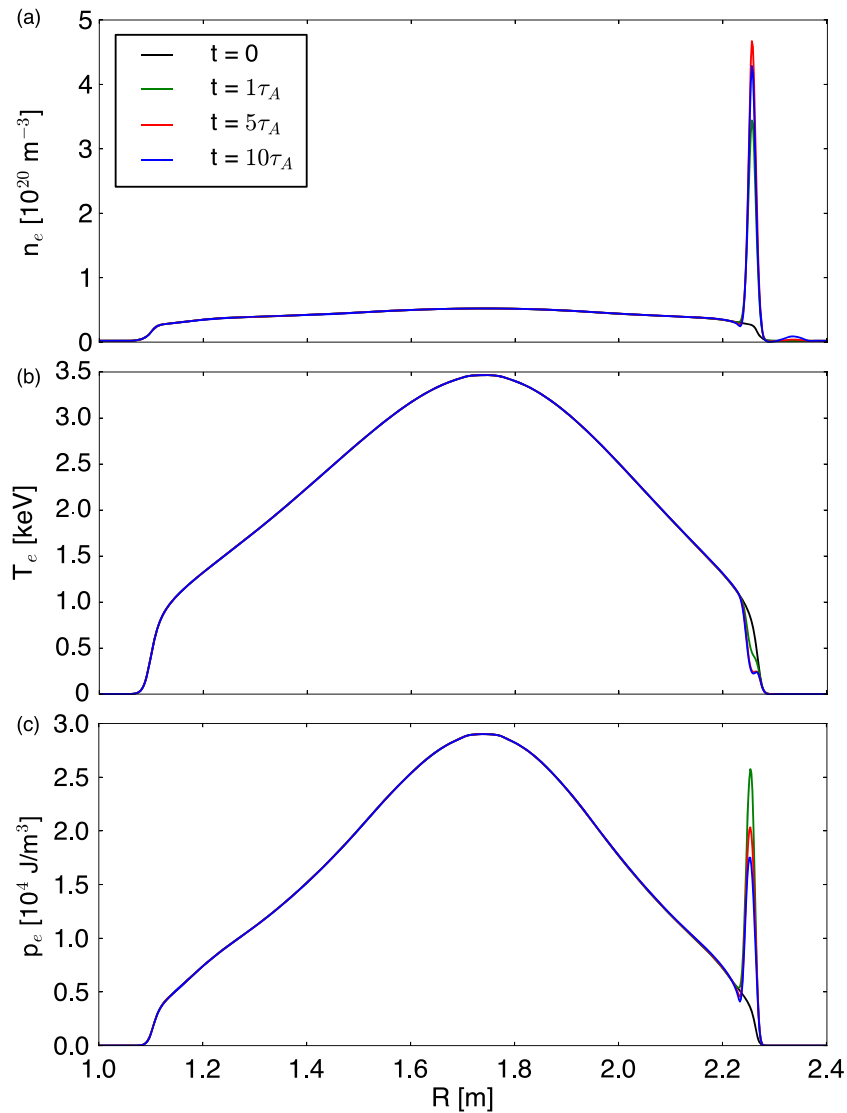
Figure 16. Radial profiles along the midplane $Z = 0$ and $\varphi = 0$ for (*a*) electron density, (*b*) electron temperature, and (*c*) electron pressure at multiple times during the pellet ablation process.

simulation for 60 Alfven times, over which time the pellet moves about 2 cm at the given velocity.

During the simulation the pellet ablates with evolving time, causing the pellet density cloud to spread, while the pellet size shrinks. Figure 14 shows the poloidal spread of the pellet density cloud over time. At $1\tau_A$ (left panel) the pellet has just been injected at the outboard midplane and starts ablating. With progressing time the cloud spreads toroidally and poloidally along the flux surfaces. Later in time (right panel) the spread of the cloud has rotated somewhat clockwise due to the $E \times B$ rotation of the plasma. At that time the pellet has moved about 2 cm radially inwards, which is hardly noticeable in the figure though.

The pellet-rate, as calculated consistently by the ablation model during the simulation, is shown in figure 15 by the red line. Very early on the pellet-rate peaks, but then saturates. The black line in the figure shows the pellet radius which is decreasing very slowly. By the end of the simulation about 13% of the pellet volume has been ablated.

Like in the linear-2D cases, the pellet causes a local peak in the electron density, as can be seen in figure 16(*a*), but here the peak density and background plasma evolve in correlation with the pellet-rate. The peak density reaches a maximum early on but then saturates around 3.5×10^{20} m^{-3}. The electron temperature drops significantly inside the pellet ablation cloud due to dilution cooling, as shown in figure 16(*b*), while the resulting electron pressure still peaks strongly as found in figure 16(*c*). This matches with the general expectations of pellet ablation and has been observed in pellet injection experiments.

Similar to figure 3 the shown figure, figure 17, gives the poloidal magnetic field of the nonlinear simulation at various times throughout the discharge. The magnetic field shows the modes exited by the pellet perturbation without the overwhelming effect of the pellet's localized density. As can be seen, similar to the process discussed in figure 3, at first the pellet excites a mode on the ablation flux surface at the pellet injection location. The perturbation spreads quickly along the
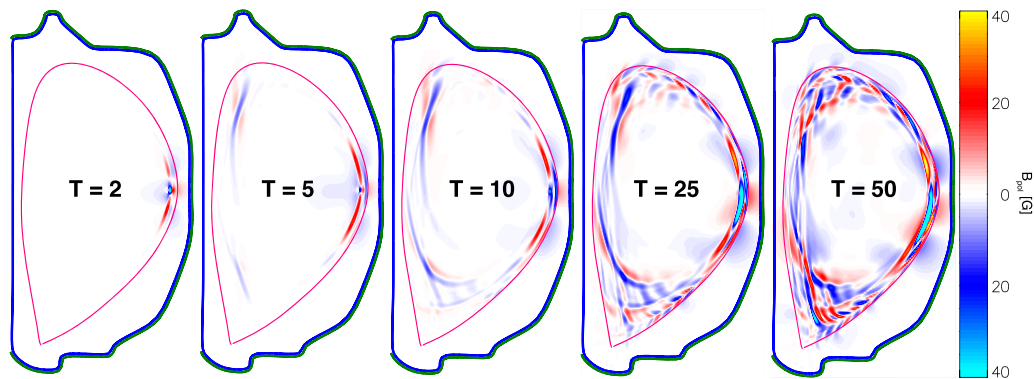
Figure 17. Poloidal magnetic field in the poloidal cross-section at $\varphi = 0$ for multiple times during the pellet ablation process. Not that all figures are on the same colorbar scale.
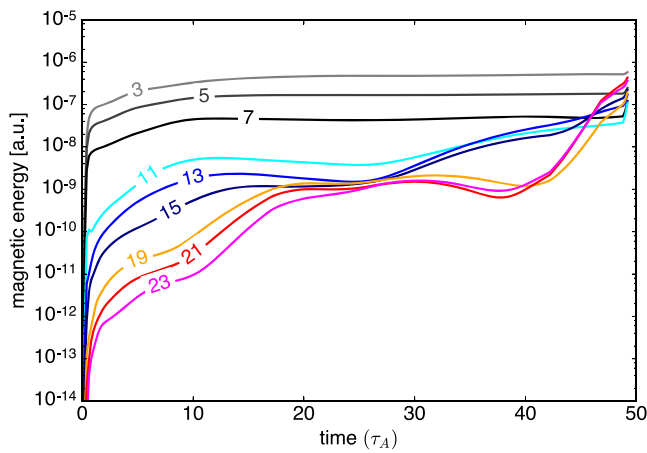
Figure 18. Time evolution of the magnetic energy for low order toroidal modes (gray colors), intermediate-*n* toroidal modes (blue colors), and high-*n* toroidal modes (red colors). The respective mode numbers *n* are given by the inline labels. Note that the *y*-axis is on a log scale.

flux surface, see $T = 10\tau_A$. Later on, see $T = 25\tau_A$, several modes located further towards the edge are excited, which then grow. Around $T = 50\tau_A$ these ELMs have grown considerably and dominate the mode spectrum.

The main result of the 3D nonlinear simulation of discharge 178555 at 3055 ms is that a pellet with radius $r_p = 0.72$ mm triggers an ELM within 50 Alfven times after the ablation begins; the result is presented in figure 18. The figure shows the magnetic energy of the spectrum of toroidal modes over time. The modes are grouped in three categories: the low order toroidal modes, $n = 3, 5, 7$ are shown by the gray colors, the intermediate-*n* toroidal modes, $n = 11, 13, 15$, which are typically associated with peeling modes, are shown by the blue colors, and the high-*n* toroidal modes, $n = 19, 21, 23$, which are typically associated with ballooning modes, are shown by the red colors. Note that the *y*-axis is on a log-scale. Early on all mode energies rise due to the initial perturbation caused by the pellet. But, around 20 Alfven times the magnetic energies of all modes have more or less saturated. Then, around 30 Alfven times the magnetic energy of all intermediate-*n* modes starts to rise significantly, indicating that these

modes are growing strongly. During that time the low-*n* and high-*n* modes remain stable; the magnetic energy of the high-*n* modes even decreases. After 40 Alfven times the magnetic energy of all high-*n* modes starts to increase quickly, exceeding the energy of all other modes around 50 Alfven times. This shows that the pellet first causes peeling modes to destabilize, which then in turn destabilize ballooning modes, by transferring mode energy [36], resulting in an ELM instability. The pellet has successfully triggered an ELM in this equilibrium. Note that a 3D nonlinear simulation of the same equilibrium without pellet injection remains stable with negligible magnetic energies for all modes. The pellet size here exceeds the critical pellet size threshold found in section 3.1, so this result is consistent with the linear simulations discussed above.

6. Conclusions

Using linear-2D M3D-C1 simulations we are able to determine the critical pellet size threshold for ELM triggering in a low-collisionality, peeling limited discharges. For multiple pellet sizes linear simulations were run for a wide range of toroidal mode numbers, sampling low-, intermediate- to high-*n* toroidal modes. The most unstable mode is found, and, by fitting the linear growth rates of the most unstable mode for all considered pellet sizes, the critical threshold is given by the pellet size where the growth rate crosses into positive. For discharge 178555 at 3055 ms the critical pellet size threshold $r_{crit} = 0.7018$ mm is found. So far all linear simulations are run in single fluid mode. In future work we will add two-fluid simulations to the linear-2D approach to include diamagnetic terms, which affect pedestal stability as well.

A fully 3D nonlinear M3D-C1 simulation of the same equilibrium confirms that a pellet of size $r_p = 0.72$ mm successfully triggers an ELM by first destabilizing intermediate-*n* peeling modes, which then in turn destabilize high-*n* ballooning modes shortly after. The 3D nonlinear simulation includes a much more realistic pellet model than the linear simulations. The pellet ablates over time while it moves radially inwards. The pellet density cloud spreads along flux surfaces, causing a significant reduction in electron temperature due to dilution cooling, while the electron pressure still peaks. While extensive parameter scans in 3D

nonlinear runs are not practical due to their computational expense, this result is consistent with our linear parameter scans, giving greater confidence to those results.

Relying further on linear-2D simulations, multiple poloidal pellet injection locations are considered, while maintaining the radial flux surface location of the pellet. It is found that the outboard midplane as well as an upper $60°$ location are favorable for pellet ELM triggering. On the other hand, locations near the upper and lower x-points are the most unfavorable locations. The inboard midplane shows about twice the critical threshold size as the outboard midplane; so does injection around $300°$. Note that the linear code used here does not account for the particle drift of the ablated material, and therefore the pellet size actually refers to the plasma perturbation size.

Published results from JOREK and JET indicate that a vertical HFS location is more favorable for pellet injection. On the other hand, as shown here, plasma conditions play a crucial role in the effectiveness of pellets to trigger ELMs. The simulations by JOREK were conducted in high-collisionality plasmas, as were the ELM triggering and pacing experiments at that time. The results by JET span a wide range of electron density and temperature, but do not distinguish by collisionality. The difference between the shown simulations and the published results could be due to drifts, which carries pellet material, so that much more pellet material reaches the critical location for ELM triggering for a pellet injected from the HFS than for one injected from the LFS. As machines gets larger, the same phenomenon is likely to play a significant role for ELM pacing, where small slow pellets are used to trigger ELMs. The entire matter indicates an issue for ITER, which is designed to inject pellets around $280°$. It is likely that, for injection near $280°$ the drift would be mainly outwards, in which case the concern is even more valid. Clearly more experimental and theoretical studies are necessary.

Using the procedure outlined earlier, the critical pellet size threshold for ELM triggering is determined for multiple times during discharge 178555 and compared against ELM triggering events in the respective experiment. In all cases the simulated threshold separates events where a small pellet fails to trigger an ELM in the experiment from events where a pellet (small or big) successfully triggers an ELM. Despite the limitations of linear-2D simulations, this result shows good agreement with experimental observation. Further experiments are currently underway, and will be followed up by ongoing modeling and simulation work in the future.

In agreement with the hypothesis for pellet ELM triggering, further linear simulations confirm that linear growth rates are significantly larger when an equilibrium operates closer to the ballooning branch compared to the original equilibrium for the same pellet size. On the other hand, the same pellet fails to trigger an ELM for an equilibrium that operates further away from the ballooning branch. This result suggests that pellet ELM triggering in ITER could be challenging due to ITER's expected low-collisionality, strongly peeling-limited operational regime. In future work we will use linear M3D-C1 simulations to determine a critical pellet size threshold for modeled ITER discharges and predict the required pellet size for the ITER pellet pacing system.

ORCID iDs

A. Wingen ⬡ https://orcid.org/0000-0001-8855-1349
B.C. Lyons ⬡ https://orcid.org/0000-0003-3232-1581
R.S. Wilcox ⬡ https://orcid.org/0000-0003-1369-1739
S.C. Jardin ⬡ https://orcid.org/0000-0001-6390-6908

References

[1] Loarte A. *et al* (the ITPA Scrape-Off Layer, and Divertor Physics Topical Group) 2007 Chapter 4: power and particle control *Nucl. Fusion* **47** S203–63
[2] Pitts R.A. *et al* 2011 Physics basis and design of the ITER plasma-facing components *J. Nucl. Mater.* **415** S957–64
[3] Kukushkin A.S., Pacher H.D., Federici G., Janeschitz G., Loarte A. and Pacher G.W. 2003 Divertor issues on ITER and extrapolation to reactors *Fusion Eng. Des.* **65** 355–66
[4] Loarte A. *et al* 2003 Characteristics of type I ELM energy and particle losses in existing devices and their extrapolation to ITER *Plasma Phys. Control. Fusion* **45** 1549–69
[5] Evans T.E. *et al* 2004 Suppression of large edge-localized modes in high-confinement DIII-D plasmas with a stochastic magnetic boundary *Phys. Rev. Lett.* **92** 235003
[6] Liang Y. *et al* 2007 Active control of type-I edge-localized modes with $n = 1$ perturbation fields in the JET tokamak *Phys. Rev. Lett.* **98** 265004
[7] Suttrop W. *et al* 2011 First observation of edge localized modes mitigation with resonant and nonresonant magnetic perturbations in ASDEX Upgrade *Phys. Rev. Lett.* **106** 225004
[8] Evans T.E. *et al* 2013 3D vacuum magnetic field modelling of the ITER ELM control coil during standard operating scenarios *Nucl. Fusion* **53** 093029
[9] Lang P.T. *et al* 2013 ELM control strategies and tools: status and potential for ITER *Nucl. Fusion* **53** 043004
[10] Baylor L.R. *et al* 2013 Reduction of edge-localized mode intensity using high-repetition-rate pellet injection in tokamak H-mode plasmas *Phys. Rev. Lett.* **110** 245001

[11] Baylor L.R. *et al* 2013 Reduction of edge localized mode intensity on DIII-D by on-demand triggering with high frequency pellet injection and implications for ITER *Phys. Plasmas* **20** 082513

[12] Bortolon A. *et al* 2016 High frequency pacing of edge localized modes by injection of lithium granules in DIII-D H-mode discharges *Nucl. Fusion* **56** 056008

[13] Lang P.T. *et al* (the ASDEX Upgrade Team) 2004 ELM pace making and mitigation by pellet injection in ASDEX Upgrade *Nucl. Fusion* **44** 665–77

[14] Lang P.T. *et al* (JET EFDA Contributors) 2011 ELM pacing investigations at JET with the new pellet launcher *Nucl. Fusion* **51** 033010

[15] Lang P.T. *et al* (JET-EFDA Contributors) 2013 ELM pacing and trigger investigations at JET with the new ITER-like wall *Nucl. Fusion* **53** 073010

[16] Sauter O., Angioni C. and Lin-Liu Y.R. 1999 Neoclassical conductivity and bootstrap current formulas for general axisymmetric equilibria and arbitrary collisionality regime *Phys. Plasmas* **6** 2834

[17] Futatani S. *et al* 2014 Non-linear MHD modelling of ELM triggering by pellet injection in DIII-D and implications for ITER *Nucl. Fusion* **54** 073008

[18] Baylor L.R. *et al* 2007 Comparison of deuterium pellet injection from different locations on the DIII-D tokamak *Nucl. Fusion* **47** 1598–606

[19] Terranova D., Garzotti L., Pégourié B., Nehme H., Frigione D., Martini S., Giovannozzi E. and Tudisco O. 2007 Pellet ablation and mass deposition in FTU: analysis of vertical and low field side injection experiments *Nucl. Fusion* **47** 288–96

[20] Garzotti L. *et al* 2010 Observation and analysis of pellet material ∇B drift on MAST *Nucl. Fusion* **50** 105002

[21] ITER Physics Basis Editors, ITER Physics Expert Group Chairs, Co-Chairs, ITER JointCentral Team, and Physics Integration Unit 1999 Chapter 1: overview and summary *Nucl. Fusion* **39** 2137

[22] Wilcox R.S. *et al* 2021 Pellet ELM triggering in DIII-D with low collisionality, peeling-limited pedestals *Proc. 28th IAEA Fusion Energy Conf.* (Nice, France 10-15 May 2021) (https://conferences.iaea.org/event/214/contributions/17148)

[23] Jardin S.C., Ferraro N., Breslau J. and Chen J. 2012 Multiple timescale calculations of sawteeth and other global macroscopic dynamics of tokamak plasmas *Comput. Sci. Discovery* **5** 014002

[24] Ferraro N.M., Jardin S.C. and Snyder P.B. 2010 Ideal and resistive edge stability calculations with M3D-C1 *Phys. Plasmas* **17** 102508

[25] Ferraro N.M., Lyons B.C., Kim C.C., Liu Y.Q. and Jardin S.C. 2019 3D two-temperature magnetohydrodynamic modeling of fast thermal quenches due to injected impurities in tokamaks *Nucl. Fusion* **59** 016001

[26] Sovinec C.R. *et al* (NIMROD Team) 2004 Nonlinear magnetohydrodynamics simulation using high-order finite elements *J. Comput. Phys.* **195** 355–86

[27] Sovinec C.R. and King J.R. (NIMROD Team) 2010 Analysis of a mixed semi-implicit/implicit algorithm for low-frequency two-fluid plasma modeling *J. Comput. Phys.* **229** 5803–19

[28] Lyons B.C., Kim C.C., Liu Y.Q., Ferraro N.M., Jardin S.C., McClenaghan J., Parks P.B. and Lao L.L. 2019 Axisymmetric benchmarks of impurity dynamics in extended-magnetohydrodynamic simulations *Plasma Phys. Control. Fusion* **61** 064001

[29] Futatani S., Cathey A., Hoelzl M., Lang P.T., Huijsmans G.T.A. and Dunne M. (the JOREK Team, the ASDEX Upgrade Team, and the EUROfusion MST1 Team) 2021 Transition from no-ELM response to pellet ELM triggering during pedestal build-up-insights from extended MHD simulations *Nucl. Fusion* **61** 046043

[30] Lao L.L., Ferron J.R., Groebner R.J., Howl W., St. John H., Strait E.J. and Taylor T.S. 1990 Equilibrium analysis of current profiles in tokamaks *Nucl. Fusion* **30** 1035–49

[31] Ferraro N.M., Jardin S.C., Lao L.L., Shephard M.S. and Zhang F. 2016 Multi-region approach to free-boundary three-dimensional tokamak equilibria and resistive wall instabilities *Phys. Plasmas* **23** 056114

[32] Parks P.B. The ablation of light-element pellets with a kinetic treatment for penetration of plasma electrons through the ablation cloud *Phys. Plasmas* (unpublished)

[33] Lennholm M. *et al* (JET Contributors) 2021 Statistical assessment of ELM triggering by pellets on JET *Nucl. Fusion* **61** 036035

[34] Snyder P.B. *et al* 2002 Edge localized modes and the pedestal: a model based on coupled peeling-ballooning modes *Phys. Plasmas* **9** 2037

[35] Meneghini O. *et al* 2015 Integrated modeling applications for tokamak experiments with OMFIT *Nucl. Fusion* **55** 083008

[36] Dominski J. and Diallo A. 2020 Identification of a network of nonlinear interactions as a mechanism triggering the onset of edge localized modes *Plasma Phys. Control. Fusion* **62** 095011